This is the accepted version of the paper:

Dunić V, Matsui R, Takeda K, Živković M. Phase-field damage simulation of subloop loading in TiNi SMA. International Journal of Damage Mechanics. 2024;0(0). Copyright © 2024 (Sage Publishing). DOI:10.1177/10567895241245859

PHASE-FIELD DAMAGE SIMULATION OF SUBLOOP LOADING IN TiNi SMA

Vladimir Dunić[1], Ryosuke Matsui[2], Kohei Takeda[2], Miroslav Živković[1]

[1] University of Kragujevac, Faculty of Engineering, Serbia

[2]Aichi Institute of Technology, Toyota, Japan

Abstract

In practical applications, TiNi shape memory alloys (SMAs) exhibit behavior that can pose a challenge with current constitutive models and their implementations in finite element method (FEM) software. TiNi SMA devices typically operate in the forward or reverse martensitic transformation regime, which is known as subloop loading. During such cyclic loading–unloading, the hysteresis stress–strain loop changes because of material damage, which can be considered the fatigue of TiNi SMAs. During both the loading and unloading processes, the stress plateau decreases. At the same time, the accumulated (residual) martensitic transformation strain increases. In this study, the experimental investigation results and observations of the aforementioned phenomena are presented. Next, the phase-field damage model is employed, along with a modified Lagoudas constitutive model, to simulate the change in stress–strain hysteresis. Furthermore, a fatigue function is used to simulate the accumulation of martensitic transformation strain. The experimental stress–strain response is compared with the simulation results, and good quantitative and qualitative agreement is obtained. The damage and martensitic volume fraction with respect to strain are discussed for full-loop and subloop loading. The observations and conclusions, as well as open questions, are presented. Possible directions for future research are provided.

Keywords: subloop loading, shape memory alloys, TiNi alloy, phase-field damage model, fatigue function

1 Introduction

Shape memory alloys (SMAs) have long piqued the interest of scientists, engineers, and engineering companies because of their specific thermomechanical characteristics. When an SMA is subjected to stress and/or a temperature change, diffusionless martensitic phase transformation occurs in either a forward or reverse direction, resulting in superelasticity or a shape memory effect. Because of this possibility, SMA attracts technologically innovative applications. The shape memory effect phenomenon, which can be observed when the material is below the austenitic transformation temperature, inspired the name SMA. The same material exhibits a superelasticity effect at a temperature above the austenitic finish. The thermomechanical behavior is related to the diffusionless phase transformation between a high-temperature, high-symmetry austenite and a low-temperature, low-symmetry martensite [1].

In particular, Ti–Ni binary SMAs (TiNi SMAs) exhibit superior recovery stress and strain and long fatigue life, resulting in their widespread application compared with other series of SMAs. TiNi SMAs have numerous industrial applications, including mechanical sensors and actuators in aerospace [2], civil [3], automotive [4, 5], and wind energy [6] industries. Some TiNi SMA devices are designed to operate in the martensitic transformation regime, where the loading–unloading conditions remain constant. These loading–unloading conditions are considered to be subloop loading. Figure 1 shows a stress–temperature phase diagram for a typical TiNi SMA, where the superelasticity phenomenon is observed at a constant temperature T (vertical line). In subloop loading, the stress changes in the martensitic and reverse transformation regions, indicated by the filled areas in Figure 1, result in incomplete martensitic and reverse transformations. By investigating the stress–strain response to subloop loading, it was observed that the behavior is strongly related to the number of cycles, which is impractical for application because a stable behavior is required [7]. In the stress–strain response, hysteresis is observed because of frictional effects inside the material, which should be described using phenomenological models [7]. In addition to stress and strain, an increase in accumulated (residual) transformation strain can be observed due to cyclic loading [8].

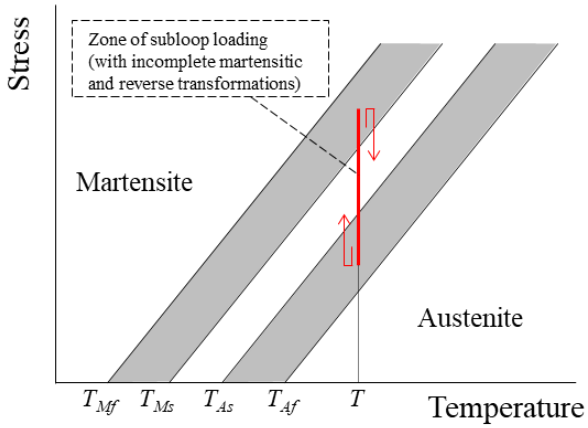

Figure 1 Phase diagram of superelasticity phenomena under isothermal loading–unloading conditions

Phenomenological constitutive models have been proposed to predict complex thermomechanical behavior under various loading and boundary conditions. In their study [9], Müller and Xu investigated the description of inner loops during superelastic behavior. They used the polynomial Landau–Devonshire theory and compared the model with the experimental results. Ortín [10] and Boyd and Lagoudas [11] also successfully considered subloops using the Preisach model. Tanaka et al. [8] and Tanaka and Nagaki [12] analyzed subloops and proposed a model with assumed phase transformation kinetics. Different subloop aspects were treated by Tobushi et al. [13], where plateaus in stress–strain hysteresis in TiNi SMAs were discussed. In [7], a constitutive model previously proposed by Savi et al. [14], Baêta-Neves et al. [15], and Paiva et al. [16] is used. They compared the numerical and experimental results and showed that they were in close agreement. Phillips et al. [17] investigated internal damage in a TiNi SMA and noticed that fatigue evolved nonlinearly. Rapid damage is associated with irrecoverable strain accumulation. Scalet et al. [18] investigated the behavior of TiNi SMAs when the transformation direction is changed in a mixed-phase state. They found that TiNi SMAs can memorize previous states, as in [19]. They explained the phenomenon in a material as an alteration of the material microstructure [20] controlled by a critical threshold energy value. They assumed that the same energy level state was achieved after a series of loadings. They also suggested that conventional TiNi SMAs can be modeled without considering irrecoverable strains and damage when the number of actuation cycles is relatively low.

Ren et al. [21] investigated the behavior of NiTi wires subjected to cyclic loading. They used a modified Lagoudas model that considers the slopes of phase transformation lines, and the residual strain is cycle-dependent. In his PhD thesis, Wang [22] generalized the Zaki–Moumni SMA model to describe cyclic pseudoelasticity with four fundamental characteristics: large residual strain, degeneration of pseudoelasticity and hysteresis loop, rate dependence, and evolution of phase transformation of polycrystalline SMAs. Wang et al. [23] used molecular dynamics to investigate the superelasticity of NiTi SMAs subjected to cyclic loading. They found that superelasticity degeneration occurs and residual strain accumulates progressively with an increasing number of cycles. Furthermore, Xiao et al. [24] and [25] established a phenomenological constitutive model for the cyclic behavior of superelastic NiTi SMAs that can capture superelasticity degradation. Moreover, in [26], Xiao et al. experimentally and numerically investigated multiple cases of cyclic loadings on superelastic NiTi SMAs. Mechanical instability was used in the model to reproduce transformation patterns under tensile stress states. Xie et al. [27] developed a three-dimensional (3D) phase-field model for NiTi SMA single crystals to simulate the cyclic phase transition. They found that NiTi SMAs exhibit localized deformation and local softening. In further investigation, Xie et al. [28] proposed a new thermomechanical phase-field model based on a previously developed isothermal phase-field model [27]. They showed that cyclic superelasticity degradation and its dependence on the loading rate and level can be captured. Choi et al. [29] proposed an integrated unified elastic–viscoplastic fatigue and creep damage model to simulate cyclic softening and creep–fatigue interaction damage. They integrated the creep and fatigue damage model into the viscoplasticity damage model and compared the obtained results with those of the experimental investigation. Kan et al. [30] investigated the stress–strain response, temperature, and dissipation energy in superelastic NiTi SMAs as the number of cycles increased. They revealed path-dependent functional fatigue, which increases with loading frequency. Kan et al. [31] experimentally investigated the functional degeneration of NiTi SMA rods under cyclic loading–unloading. Kan et al. [32] also presented the experimental and theoretical evolution of the superelasticity of NiTi SMA helical springs under cyclic deformation.

Until now, some phenomenological models have been able to capture subloop behavior and consider accumulated martensitic transformation strain. The proposed solutions are based on different mathematical models and provide satisfactory results for special cases. However, a comprehensive solution that can cover all subloop loading cases and the accumulation of transformation strain remains a topic of interest for scientists and is essential for the use of TiNi SMAs in engineering solutions. The phase-field damage model (PFDM) has recently attracted attention as a universal solution. By considering damage to materials as an additional degree of freedom, the behavior of structures under cyclic loading can be observed. The first implementation and application of the PFDM for TiNi SMAs were presented in two studies [33,34] using different phenomenological constitutive models. In the first study, the Lagoudas model was used, whereas the Drucker–Prager yield function was employed in the second study. In both studies, fatigue functions were proposed [35].

In this study, the authors experimentally investigated TiNi SMAs under subloop loading conditions and proposed the PFDM as a functional solution for the simulation of subloop hysteresis, as well as the accumulation of damage and its relationship with the accumulated martensitic volume fraction and residual transformation strain. The modified Lagoudas model [36,37] was used as the base for the PFDM implementation. The proposed modifications are reviewed for completeness, and details related to the Boyd–Lagoudas hardening function are presented [38]. Next, the PFDM theory, along with the derivation of a fatigue function, is presented. Thermomechanical coupling is not considered in this study because the experimental investigation is performed at low strain rates. Thus, the temperature of the material is assumed to be constant. The TiNi SMA is first investigated under full-loop loading–unloading conditions. Subloop loading–unloading is then performed, and the stress–strain response is obtained. Both tests are simulated, and the material parameters are calibrated. The comparison of the stress–strain response, the obtained parameters, and the relationship between the accumulated damage and martensitic volume fraction are discussed in detail, with open questions for future research. Within

this scope, this study not only provides answers to some questions but also opens new questions that require further research.

2 Theory

2.1 TiNi SMA constitutive model

Previous experience with the constitutive model presented in Lagoudas's paper [38], as well as its implementation in finite element method (FEM) software [36], imply that it is one of the phenomenological models that can be successfully modified to capture the subloop loading behavior in conjunction with the PFDM. Therefore, this subsection provides an overview of the main constitutive model theory, and the proposed modifications [36,37], along with the hardening function employed for simulations [38], are reviewed. The TiNi SMA model is derived on the basis of a Gibbs free energy function, g, extended by a transformation hardening function, $f(\xi)$, that depends on a martensitic volume fraction, ξ. The model is explicitly expressed, as in Qidwai and Lagoudas [1]:

$$g\left(\boldsymbol{\sigma},T,\xi,\mathbf{e}_{tr}\right)=-\frac{1}{2\rho}\boldsymbol{\sigma}:\mathcal{M}:\boldsymbol{\sigma}-\frac{1}{\rho}\boldsymbol{\sigma}:\left[\boldsymbol{\alpha}(T-T_0)+\mathbf{e}_{tr}\right]+ \\ +c\left[(T-T_0)-T\ln\left(\frac{T}{T_0}\right)\right]-s_0T+u_0+\frac{1}{\rho}f(\xi) \tag{1}$$

Two internal state variables define the constitutive model: the martensitic volume fraction ξ and the martensitic transformation strain $\mathbf{e}_{tr}$. The variables $\boldsymbol{\sigma}$ and T denote the total stress and the temperature of the material, respectively, $\mathcal{M}$ represents the effective compliance tensor, $\boldsymbol{\alpha}$ denotes the effective thermal expansion coefficient tensor, T represents the current temperature of the material, T_0 denotes the reference temperature, c represents the effective specific heat, s_0 denotes the effective specific entropy, u_0 denotes the effective specific internal energy, and ρ denotes the density of the material. The main assumption for the derivation of this constitutive model is that the change in martensitic transformation strain $\mathbf{e}_{tr}$ is strictly because of a change in the amount of martensitic volume fraction ξ as follows [1]:

$$\dot{\mathbf{e}}_{tr}=H\mathbf{n}_{tr}\dot{\xi}\,, \tag{2}$$

where H represents the value of the maximal transformation strain and $\mathbf{n}_{tr}$ denotes the transformation direction vector [36-38]. By introducing the Legendre transformation, as described in [39],

$$g=u-sT-\frac{1}{\rho}\boldsymbol{\sigma}:\mathbf{e}\,, \tag{3}$$

where u represents the internal energy, s represents the specific entropy, and $\mathbf{e}$ represents the total strain tensor. The first law of thermodynamics can be expressed as follows [36,38,39]:

$$\rho\dot{u}=\boldsymbol{\sigma}:\mathbf{e}-div\left(\mathbf{q}\right)+\rho q\,, \tag{4}$$

where $\mathbf{q}$ represents the heat flux and q represents the heat source of the added thermal energy. When we substitute Eq. (4) into the Clausius–Duhem equation [38],

$$\rho\dot{s}T+div\left(\mathbf{q}\right)-\rho q\geq 0\,. \tag{5}$$

The Clausius–Planck inequality can be obtained as follows [36,38,39]:

$$\mathcal{D}_{int} = \frac{1}{\rho}\boldsymbol{\sigma} : \mathbf{e} - \dot{u} + T\dot{s} \geq 0 . \tag{6}$$

The time derivative of the Gibbs free energy is given by [36,38]

$$\dot{g} = \dot{u} - \dot{s}T - s\dot{T} - \frac{1}{\rho}\dot{\boldsymbol{\sigma}} : \mathbf{e} - \frac{1}{\rho}\boldsymbol{\sigma} : \dot{\mathbf{e}} \tag{7}$$

can be substituted into Eq. (5), yielding the following [36,38]:

$$-\rho\dot{g} - \dot{\boldsymbol{\sigma}} : \mathbf{e} - \rho s\dot{T} \geq 0 . \tag{8}$$

The total derivative of the Gibbs free energy is [36,38]

$$\dot{g} = \frac{\partial g}{\partial \boldsymbol{\sigma}} : \dot{\boldsymbol{\sigma}} + \frac{\partial g}{\partial T} : \dot{T} + \frac{\partial g}{\partial \mathbf{T}} : \dot{\mathbf{T}} + \frac{\partial g}{\partial \mathbf{e}_{tr}} : \dot{\mathbf{e}}_{tr} + \frac{\partial g}{\partial \xi} : \dot{\xi} , \tag{9}$$

and when it is substituted into Eq. (8), the following is obtained:

$$-\rho\left(\frac{\partial g}{\partial \boldsymbol{\sigma}} : \dot{\boldsymbol{\sigma}} + \frac{\partial g}{\partial T} : \dot{T} + \frac{\partial g}{\partial \mathbf{T}} : \dot{\mathbf{T}} + \frac{\partial g}{\partial \mathbf{e}_{tr}} : \dot{\mathbf{e}}_{tr} + \frac{\partial g}{\partial \xi} : \dot{\xi} \right) - \dot{\boldsymbol{\sigma}} : \mathbf{e} - \rho s\dot{T} \geq 0 . \tag{10}$$

The total strain tensor $\mathbf{e}$ and entropy s are defined as [36,38]

$$\mathbf{e} = -\rho\frac{\partial g}{\partial \boldsymbol{\sigma}} = \mathcal{M} : \boldsymbol{\sigma} + \boldsymbol{\alpha} : \left(T - T_0\right) + \mathbf{e}_{tr} , \tag{11}$$

$$s = -\frac{\partial g}{\partial T} = \frac{1}{\rho}\boldsymbol{\sigma} : \boldsymbol{\alpha} + c\ln\left(\frac{T}{T_0}\right) + s_0 . \tag{12}$$

From Eq. (11), it can be noticed that the total infinitesimal strain is the sum of the elastic strain $\mathbf{e}_e$, the thermal strain $\mathbf{e}_t$, and the martensitic transformation strain $\mathbf{e}_{tr}$ [36,38]:

$$\mathbf{e} = \mathbf{e}_e + \mathbf{e}_t + \mathbf{e}_{tr} . \tag{13}$$

It is now possible to show that the internal dissipation of energy is greater than or equal to zero [36,38]:

$$\mathcal{D}_{int} = -\rho\left(\frac{\partial g}{\partial \mathbf{e}_{tr}} : \dot{\mathbf{e}}_{tr} + \frac{\partial g}{\partial \xi} : \dot{\xi} \right) = \boldsymbol{\sigma} : \dot{\mathbf{e}}_{tr} + \left(-\rho\frac{\partial g}{\partial \xi} \right)\dot{\xi} \geq 0 . \tag{14}$$

Substituting Eq. (2) into Eq. (14), the general thermodynamic force Π can be obtained as follows [36,38]:

$$\mathcal{D}_{int} = \left(\boldsymbol{\sigma} : \mathbf{n}_{tr} H - \rho\frac{\partial g}{\partial \xi} \right)\dot{\xi} = \Pi\dot{\xi} \geq 0 . \tag{15}$$

For the given Gibbs free energy in Eq. (1), the explicit form of Π is [38]

$$\Pi(\boldsymbol{\sigma},T,\xi)=\boldsymbol{\sigma}:\mathbf{n}_{tr}H+\frac{1}{2}\boldsymbol{\sigma}:\Delta\mathcal{M}:\boldsymbol{\sigma}+\boldsymbol{\sigma}:\Delta\boldsymbol{\alpha}\left(T-T_0\right)-$$
$$\rho\Delta c\left[\left(T-T_0\right)-T\ln\left(\frac{T}{T_0}\right)\right]+\rho\Delta s_0 T-\rho\Delta u_0-\frac{\partial f(\xi)}{\partial\xi}\quad , \tag{16}$$

where $\Delta\mathcal{M}=\mathcal{M}^M-\mathcal{M}^A,\Delta\boldsymbol{\alpha}=\boldsymbol{\alpha}^M-\boldsymbol{\alpha}^A,\Delta c=c^M-c^A,\Delta s_0=s_0^M-s_0^A,\Delta u_0=u_0^M-u_0^A$, where the subscript A denotes the austenite phase and M denotes the martensite phase. The simplest Boyd–Lagoudas [1,11,38] hardening function $f(\xi)$ is used in this case as follows:

$$f\left(\xi\right)=\begin{cases}\frac{1}{2}\rho b^M\xi^2+\left(\mu_1+\mu_2\right)\xi, & \dot{\xi}>0\\ \frac{1}{2}\rho b^A\xi^2+\left(\mu_1-\mu_2\right)\xi, & \dot{\xi}<0\end{cases}, \tag{17}$$

where b^M,b^A,μ_1,μ_2 are the transformation strain hardening material constants [1]:

$$\begin{aligned}b^A&=-\Delta s_0\left(T_{Af}-T_{As}\right),\\ b^M&=-\Delta s_0\left(T_{Ms}-T_{Mf}\right),\\ \mu_1&=\frac{1}{2}\rho\Delta s_0\left(T_{Ms}+T_{Af}\right)-\rho\Delta u_0,\\ \mu_2&=\frac{1}{4}\rho\Delta s_0\left(T_{As}-T_{Af}-T_{Mf}+T_{Ms}\right).\end{aligned} \tag{18}$$

The transformation function Φ is introduced by Lagoudas as [38]

$$\Phi=\begin{cases}\Pi-Y; & \dot{\xi}>0\\ -\Pi-Y; & \dot{\xi}<0\end{cases}, \tag{19}$$

where Y represents the threshold value, which depends on the transformation hardening function $f(\xi)$ [38,40]:

$$Y=\frac{1}{4}\rho\Delta s_0\left(T_{Ms}+T_{Mf}-T_{Af}-T_{As}\right). \tag{20}$$

The decomposition of the total stress on the deviatoric $\mathbf{S}'$ and the mean part σ_m is [41]

$$\boldsymbol{\sigma}=\mathbf{S}'+\sigma_m\mathbf{I}. \tag{21}$$

It can be used in Eq.(19) with an approximation that the proposed transformation direction $\mathbf{n}_{tr}$ in Eq. (2) is constant and equal to the trial value from the beginning of the time step [41,42]. The transformation function is derived in a scalar form as [36]:

$$\Phi=\begin{cases} H\bar{S}+\dfrac{1}{2}\left(\dfrac{1}{3}\bar{S}^2\left(\dfrac{1}{G^M}-\dfrac{1}{G^A}\right)+3\sigma_m^2\left(\dfrac{1}{c_m^M}-\dfrac{1}{c_m^A}\right)\right)+3\sigma_m\left(\alpha^M-\alpha^A\right)\Delta T+ & ;\dot{\xi}>0 \\ +\rho\Delta s_0\left(T-T_{Ms}\right)-\rho\Delta s_0\left(T_{Ms}-T_{Mf}\right)\xi & \\ -\mathbf{S}'_*:\mathbf{e}_{tr}\dfrac{H}{\bar{e}_{tr}}+3G\Delta\xi H^2-\dfrac{1}{2}\left(\dfrac{1}{3}\bar{S}^2\left(\dfrac{1}{G^M}-\dfrac{1}{G^A}\right)+3\sigma_m^2\left(\dfrac{1}{c_m^M}-\dfrac{1}{c_m^A}\right)\right) & ;\dot{\xi}<0 \\ -3\sigma_m\left(\alpha^M-\alpha^A\right)\Delta T-\rho\Delta s_0\left(T-T_{Af}\right)+\rho\Delta s_0\left(T_{Af}-T_{As}\right)\xi & \end{cases}, \quad (22)$$

where G^A and G^M denote the shear moduli for austenite and martensite, respectively, c_m^A and c_m^M denote 1/3 of the bulk moduli for the austenite and martensite phases, $\bar{S}$ denotes the von Mises equivalent stress, $\bar{e}_{tr}$ denotes the equivalent transformation strain, $\mathbf{S}'_*$ denotes the trial deviatoric stress, T_{Ms} denotes the martensite start temperature, and T_{Af} denotes the austenite finish temperature. When $\Phi<0$, an elastic response is obtained; however, for both forward and reverse phase transformations, the transformation function needs to satisfy $\Phi=0$ while $\dot{\xi}\neq 0$.

2.2 Phase-field damage modeling

In the literature [43-46], the PFDM was introduced by analyzing a bar with a constant cross-section, as shown in Figure 2. The damage variable d along the x axis of the bar can be defined for the diffusive crack topology as an exponential function [43-46]:

$$d(x)=\mathrm{e}^{-\frac{|x|}{l_c}}, \quad (23)$$

where l_c is defined as a characteristic length-scale parameter.

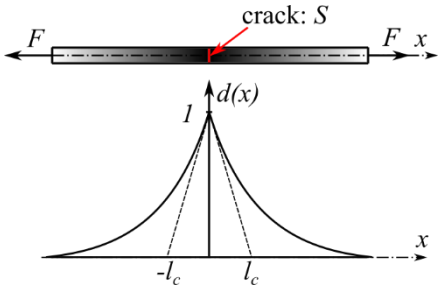

Figure 2 Bar loaded by forces F on both sides with a crack surface S in the middle: damage phase field for diffusive crack topology [44,45,47,48]

The internal potential energy density ψ is considered the sum of mechanical energy density $\psi^M(\boldsymbol{\varepsilon},d)$ and fracture surface energy density $\varphi^S(d,\nabla d)$ [33-35,49,50]:

$$\psi=\psi^M(\boldsymbol{\varepsilon},d)+\varphi^S(d,\nabla d). \quad (24)$$

The mechanical strain energy density of the virgin material ψ_0^M is multiplied by the degradation function $\theta(d)$ to define the mechanical strain energy density ψ^M as [33-35,49,50]

$$\psi^M(\mathbf{e},\xi,d)=\theta(d)\psi_0^M(\mathbf{e},\xi)=\theta(d)\boldsymbol{\sigma}_0(\xi):\mathbf{e}, \tag{25}$$

where $\boldsymbol{\sigma}_0(\xi)$ denotes the Cauchy stress tensor of an undamaged solid. Similarly, the "damaged" Cauchy stress $\boldsymbol{\sigma}(\xi)$ is expressed as follows [47,48,51]:

$$\boldsymbol{\sigma}(\xi,d)=\theta(d)\boldsymbol{\sigma}_0(\xi). \tag{26}$$

The fracture surface energy Φ^S at the crack surface S is defined as [33-35,49,50]

$$\Phi^S=\int_S f(\bar{\alpha})G_c dS\approx\int_V f(\bar{\alpha})G_c\gamma(d,\nabla d)dV=\int_V\varphi^S(d)dV, \tag{27}$$

where the regularized crack surface functional for multi-dimensional solids is obtained in the same manner as that given in the literature [33,34,43,44]:

$$S(d)=\int_V f(\bar{\alpha})\gamma(d,\nabla d)dV. \tag{28}$$

The fracture surface energy density dissipated by the formation of the crack is defined as follows:

$$\varphi^S(d)=f(\bar{\alpha})G_c\gamma(d,\nabla d). \tag{29}$$

In the previous equations, G_c denotes the Griffith-type critical fracture energy release rate, also known as the fracture toughness of the material, described as the amount of energy required to produce a unit area of the fracture surface, and γ denotes a crack surface density function per unit volume defined as [33,35,43-46,49,50]

$$\gamma(d,\nabla d)=\frac{d^2}{2l_c}+\frac{l_c}{2}|\nabla d|^2, \tag{30}$$

where ∇ denotes the gradient operator. Cyclic loading causes more damage, which is captured by the fatigue function $f(\bar{\alpha})$ [33-35]. This function degrades the material toughness with respect to the fatigue history variable. The increment of the history variable can be defined as [31-35]

$$\Delta\bar{\alpha}(t)=\int_t^{t+\Delta t}H(\alpha\dot{\alpha})|\dot{\alpha}|d\tau, \tag{31}$$

where $H(\alpha\dot{\alpha})$ denotes the Heaviside step function [31-35]:

$$H(\alpha\dot{\alpha})=\begin{cases}1, & \alpha\dot{\alpha}\geq 0 \text{ for loading}\\ 0, & \text{otherwise for unloading}\end{cases}. \tag{32}$$

The fatigue history variable α is defined as [31-35]

$$\alpha=\psi^M, \tag{33}$$

resulting in

$${}^{t+\Delta t}\bar{\alpha}={}^{t}\bar{\alpha}+\Delta\bar{\alpha}, \tag{34}$$

whereas the fatigue function is [33]

$$f\left(\bar{\alpha}\right)=\begin{cases}1 & \text{if} \quad \bar{\alpha}\le\alpha_T\\ \left(\dfrac{2\alpha_T}{\bar{\alpha}+\alpha_T}\right)^2 & \text{if} \quad \bar{\alpha}>\alpha_T\end{cases}. \tag{35}$$

Here, α_T denotes a threshold value below which the fracture energy remains unaffected. It is adopted according to the literature [33]:

$$\alpha_T=\frac{G_V}{12}. \tag{36}$$

Threshold value in Eq. (36) controls the accumulation of the mechanical strain energy responsible for the damage. Damage occurs from the beginning of loading because of the increase in elastic strain energy, which is a reason for fracture in high cyclic fatigue cases when materials do not exhibit inelastic strains. When the accumulated mechanical strain energy ${}^{t+\Delta t}\bar{\alpha}$ is higher than the threshold value α_T, the fatigue function in Eq. (35) affects the fracture energy in Eq. (29) in a way that decreases it below its initial value, which accelerates the damage and finally leads to fracture. The fatigue life of the SMA depends on the accumulated elastic strain energy, whereas the inelastic strain and the forward and reverse martensitic transformation do not influence the damage. Furthermore, in the case of cyclic loading up to the same total strain value, according to the model, the fatigue life tends to infinity, which can be observed in the experimental investigation of NiTi SMAs, where the fatigue life is up to several tens of thousands of cycles.

The total internal potential energy W_{int} functional is defined as [33-35,47-51]

$$W_{int}=\int_V \psi dV=\int_V\left\{\theta\left(d\right)\boldsymbol{\sigma}_0(\xi):\mathbf{e}+f\left(\bar{\alpha}\right)G_V\left[\frac{d^2}{2}+\frac{l_c^2}{2}\left|\nabla d\right|^2\right]\right\}dV, \tag{37}$$

where the critical fracture energy release rate per unit volume is $G_V=\dfrac{G_c}{l_c}$. The variation in the internal potential energy over the total strain and damage is given as [47,48,51]

$$\delta W_{int}=\int_V\left(\frac{\partial\psi}{\partial\mathbf{e}}:\delta\mathbf{e}+\frac{\partial\psi}{\partial d}:\delta d\right)dV. \tag{38}$$

We can obtain [47,48,51]

$$\delta W_{int}=\int_V\left\{\boldsymbol{\sigma}:\delta\mathbf{e}+f\left(\bar{\alpha}\right)G_V\left[d\delta d+l_c^2\nabla d\nabla\delta d\right]\right\}dV. \tag{39}$$

Variation in the external potential energy W_{ext} is known as [47,48,51]

$$\delta W_{ext}=\int_V\mathbf{b}\cdot\delta\mathbf{u}dV+\int_A\mathbf{h}\cdot\delta\mathbf{u}dA, \tag{40}$$

where $\mathbf{b}$ represents the body force field per unit volume, $\mathbf{h}$ represents the boundary traction per unit area, and $\mathbf{u}$ represents the displacement vector. The equilibrium of the internal and external potential energies [47,48,51] is

$$\delta W_{int}=\delta W_{ext}, \tag{41}$$

$$\int_V \left\{ \boldsymbol{\sigma} : \delta\mathbf{e} + \frac{1}{2}\theta'(d)\boldsymbol{\sigma}_0 : \mathbf{e}\delta d + f(\bar{\alpha})G_V \left[d\delta d + l_c^2 \nabla d \nabla \delta d \right] \right\} dV = \\ = \int_V \mathbf{b} \cdot \delta\mathbf{u} dV + \int_A \mathbf{h} \cdot \delta\mathbf{u} dA \quad . \tag{42}$$

Using the total derivatives of the following terms and the Gauss theorem, we obtain the following [47,48,51]:

$$\int_V \{ -\left[\theta'(d)\psi_0^M + f(\bar{\alpha})G_V \left[d - l_c^2 \nabla^2 d \right] \right] \delta d - \left[Div[\boldsymbol{\sigma}] + \mathbf{b} \right] \cdot \delta\mathbf{u} \} dV + \\ + \int_A \left\{ \left[\boldsymbol{\sigma} \cdot \mathbf{n} - \mathbf{h} \right] \cdot \delta\mathbf{u} \right\} dA + \int_A \left\{ \left[f(\bar{\alpha})G_V l_c^2 \nabla d \cdot \mathbf{n} \right] \delta d \right\} dA = 0 \tag{43}$$

where $\mathbf{n}$ represents the unit outer normal to the surface A. The Neumann-type boundary conditions are as follows [47,48,51]:

$$\boldsymbol{\sigma} \cdot \mathbf{n} - \mathbf{h} = 0, \tag{44}$$

$$\nabla d \cdot \mathbf{n} = 0, \tag{45}$$

which result in the following governing balance equations [47,48,51]:

$$Div[\boldsymbol{\sigma}] + \mathbf{b} = 0, \tag{46}$$

$$f(\bar{\alpha})G_V \left[d - l_c^2 \nabla^2 d \right] + \theta'(d)\psi_0^M = 0. \tag{47}$$

2.3 FEM software implementation

In [36,52-54], the thermomechanically coupled FEM software PAK, developed at the Faculty of Engineering, University of Kragujevac, Serbia, as an in-house non-commercial software solution, was used to investigate the influence of strain rate on the stress–strain response in TiNi SMAs. However, in this study, thermomechanical coupling is not necessary, because the low strain rate loading conditions do not increase the temperature of TiNi SMAs; thus, isothermal conditions can be considered. To simulate the mechanical behavior of TiNi SMAs, the structural analysis software PAK-S [55] is used. PAK-S is a software for structural analysis based on FEM. It can be used for linear and nonlinear analyses, which include various types of constitutive models, loading and boundary conditions, elements, and iterative solvers for parallel processing. In addition, this software implements the phase-field damage modeling presented in Section 2.2. The TiNi SMA constitutive model presented in Section 2.1 is implemented to compute displacements, martensitic volume fraction, total stress, total strain, and transformation strain fields. In PAK-S, the PFDM theory presented in Section 2.2 is also implemented, and 3D multi-field elements are created to solve the fields of displacement and damage separately in a staggered solution scheme [47,48,51].

This section describes discretization using standard finite elements and Lagrange interpolation functions. The standard Galerkin method is used to derive the equilibrium equations of finite elements [47,48,51]. The displacement vector of the nodes $\mathbf{U}$ is unknown and should be determined. By grouping the terms in Eq. (42) with the displacement variation $\delta\mathbf{u}$ and damage variation δd, we obtain the energy balance equations as follows [47,48,51]:

$$\int_V \boldsymbol{\sigma} : \delta\mathbf{e} dV = \int_V \mathbf{b} \cdot \delta\mathbf{u} dV + \int_A \mathbf{h} \cdot \delta\mathbf{u} dA, \tag{48}$$

$$\int_V \left\{ \theta'(d)\psi_0 \delta d + f(\bar{\alpha}) G_V \left[d\delta d + l_c^2 \nabla d \cdot \nabla \delta d \right] \right\} dV = 0. \tag{49}$$

The displacement vector $\mathbf{u}$ at the integration point is defined as [41]

$$\mathbf{u} = \mathbf{N}^u \mathbf{U}, \tag{50}$$

where $\mathbf{N}^u$ denotes the matrix of interpolation functions [56] for the interpolation of displacement values in the nodes of the finite element located in the vector $\mathbf{U}$. The small strain vector $\boldsymbol{\varepsilon}$ at the integration point is defined as [41,49]

$$\mathbf{e} = \mathbf{B}^u \mathbf{U}, \tag{51}$$

where $\mathbf{B}^u$ (strain–displacement) denotes the matrix containing the derivatives of the interpolation functions [56]. The value of the damage field d at the integration point is given by [49,50]

$$d = \mathbf{N}^d \mathbf{d}, \tag{52}$$

where $\mathbf{N}^d$ denotes the vector of interpolation functions for the interpolation of the damage values in the nodes of the finite element, which are located in the vector $\mathbf{d}$. The local gradient of damage ∇d, which we denote by analogy with strains as $\boldsymbol{\varepsilon}^d$, is [49,50]

$$\boldsymbol{\varepsilon}^d = \nabla d = \mathbf{B}^d \mathbf{d}, \tag{53}$$

where $\mathbf{B}^d$ (damage gradient − damage) denotes the matrix containing the derivatives of the interpolation functions. We can express the variation in the displacement field $\mathbf{u}$ and the variation in the damage field d as [47,48,51]

$$\delta \mathbf{u} = \mathbf{N}^u \delta \mathbf{U}, \tag{54}$$

$$\delta d = \mathbf{N}^d \delta \mathbf{d}. \tag{55}$$

Variations in the small strain $\boldsymbol{\varepsilon}$ and the damage gradient ∇d are [47,48,51]

$$\delta \boldsymbol{\varepsilon} = \mathbf{B}^u \delta \mathbf{U}, \tag{56}$$

$$\nabla \delta d = \mathbf{B}^d \delta \mathbf{d}, \tag{57}$$

resulting in [47,48,51]

$$\delta \mathbf{U}^T \left(\mathbf{F}^u - \mathbf{R} \right) = 0, \tag{58}$$

$$\delta \mathbf{d}^T \mathbf{F}^d = 0, \tag{59}$$

where $\mathbf{R}$ represents the vector of external forces, $\mathbf{F}^u$ denotes the vector of internal forces, and $\mathbf{F}^d$ denotes the part of the internal potential energy associated with damage:

$$\mathbf{R} = \int_V \mathbf{N}^{uT} \mathbf{b} dV + \int_A \mathbf{N}^{uT} \mathbf{h} dA, \tag{60}$$

$$\mathbf{F}^u = \int_V \mathbf{B}^{uT} \boldsymbol{\sigma} dV, \tag{61}$$

$$\mathbf{F}^d = \int_V \left\{ \mathbf{N}^{dT} \theta'(d) \psi_0 + f(\bar{\alpha}) G_V \left[\mathbf{N}^{dT} d + \mathbf{B}^{dT} l_c^2 \nabla d \right] \right\} dV . \tag{62}$$

For arbitrary variations in the displacement vector $\delta\mathbf{U}$ and damage vector $\delta\mathbf{d}$, from Eqs. (58) and (59), the equilibrium equations of the finite elements are obtained as [47,48,51]

$$\mathbf{F}^u = \mathbf{R}, \tag{63}$$

$$\mathbf{F}^d = \mathbf{0}, \tag{64}$$

that is

$$\int_V \theta(d) \mathbf{B}^{uT} \boldsymbol{\sigma}_0 dV = \int_V \mathbf{N}^{uT} \mathbf{b} dV + \int_A \mathbf{N}^{uT} \mathbf{h} dA, \tag{65}$$

$$\int_V \left\{ \mathbf{N}^{dT} \theta'(d) \psi_0 + f(\bar{\alpha}) G_V \left[\mathbf{N}^{dT} d + \mathbf{B}^{dT} l_c^2 \nabla d \right] \right\} dV = \mathbf{0}. \tag{66}$$

Eqs. (65) and (66) are nonlinear functions of displacement and damage, which generally cannot be solved directly but are solved incrementally. Suppose we have known solutions at time and are looking for solutions at time, where Δt denotes the time or load step. We consider that the external forces are independent of strain and are known at each time step. We can express [41]

$${}^{t+\Delta t}\mathbf{R} = {}^{t}\mathbf{R} + \Delta\mathbf{R}, \tag{67}$$

where ${}^{t}\mathbf{R}$ and ${}^{t+\Delta t}\mathbf{R}$ denote the external forces at the beginning and end of the time step, respectively, and $\Delta\mathbf{R}$ denotes the increment in the external forces in the time step. By solving the nonlinear system of Eqs. (63) and (64) at the time $t+\Delta t$ [47,48,51],

$${}^{t+\Delta t}\mathbf{F}^u = {}^{t+\Delta t}\mathbf{R}, \tag{68}$$

$${}^{t+\Delta t}\mathbf{F}^d = \mathbf{0}, \tag{69}$$

displacement $\Delta\mathbf{U}$ and damage $\Delta\mathbf{d}$ increments in the nodes are obtained, on the basis of which the total displacements ${}^{t+\Delta t}\mathbf{U}$ and damages ${}^{t+\Delta t}\mathbf{d}$ at the end of the step are calculated as [47,48,51]

$${}^{t+\Delta t}\mathbf{U} = {}^{t}\mathbf{U} + \Delta\mathbf{U}, \tag{70}$$

$${}^{t+\Delta t}\mathbf{d} = {}^{t}\mathbf{d} + \Delta\mathbf{d}, \tag{71}$$

where we consider the known displacements and damage ${}^{t}\mathbf{d}$ from the beginning of the step. Eqs. and are linearized by expanding the vector of internal forces and the vector of internal damage energy ${}^{t+\Delta t}\mathbf{F}^d$ into the Taylor series as [47,48,51]

$${}^{t+\Delta t}\mathbf{F}^u \approx {}^{t}\mathbf{F}^u + \frac{\partial {}^{t}\mathbf{F}^u}{\partial {}^{t}\mathbf{U}} \Delta\mathbf{U}^{(1)} + \frac{\partial {}^{t}\mathbf{F}^u}{\partial {}^{t}\mathbf{d}} \Delta\mathbf{d}^{(1)}, \tag{72}$$

$${}^{t+\Delta t}\mathbf{F}^d \approx {}^{t}\mathbf{F}^d + \frac{\partial {}^{t}\mathbf{F}^d}{\partial {}^{t}\mathbf{U}} \Delta\mathbf{U}^{(1)} + \frac{\partial {}^{t}\mathbf{F}^d}{\partial {}^{t}\mathbf{d}} \Delta\mathbf{d}^{(1)}, \tag{73}$$

where $\Delta\mathbf{U}^{(1)}$ denotes the first approximation of the displacement increment and $\Delta\mathbf{d}^{(1)}$ denotes the first approximation of the damage increment. Substituting Eq. (72) into Eq. (68) and Eq. (73) into Eq. (69), we obtain the following system of coupled equations [47,48,51]:

$$\begin{bmatrix} {}^{t}\mathbf{K}^{uu} & {}^{t}\mathbf{K}^{ud} \\ {}^{t}\mathbf{K}^{du} & {}^{t}\mathbf{K}^{dd} \end{bmatrix} \begin{Bmatrix} \Delta\mathbf{U}^{(1)} \\ \Delta\mathbf{d}^{(1)} \end{Bmatrix} = \begin{Bmatrix} {}^{t+\Delta t}\mathbf{R} - {}^{t}\mathbf{F}^{u} \\ -{}^{t}\mathbf{F}^{d} \end{Bmatrix}, \tag{74}$$

where the submatrices of the tangent stiffness matrix are [47,48,51]

$${}^{t}\mathbf{K}^{uu} = \frac{\partial {}^{t}\mathbf{F}^{u}}{\partial {}^{t}\mathbf{U}} = \int_{V} \theta\left({}^{t}d\right)\mathbf{B}^{uT} \frac{\partial {}^{t}\boldsymbol{\sigma}_{0}}{\partial {}^{t}\mathbf{U}} \mathbf{B}^{u} dV \,, \tag{75}$$

$${}^{t}\mathbf{K}^{ud} = \frac{\partial {}^{t}\mathbf{F}^{u}}{\partial {}^{t}\mathbf{d}} = \int_{V} \theta'\left({}^{t}d\right)\mathbf{B}^{uT}\, {}^{t}\boldsymbol{\sigma}_{0}\mathbf{N}^{d} dV \,, \tag{76}$$

$${}^{t}\mathbf{K}^{du} = \frac{\partial {}^{t}\mathbf{F}^{d}}{\partial {}^{t}\mathbf{U}} = \int_{V} \theta'\left({}^{t}d\right)\mathbf{N}^{dT}\, {}^{t}\boldsymbol{\sigma}_{0}^{T}\mathbf{B}^{u} dV \,, \tag{77}$$

$${}^{t}\mathbf{K}^{dd} = \frac{\partial {}^{t}\mathbf{F}^{d}}{\partial {}^{t}\mathbf{d}} = \int_{V} \left\{ \left[\theta''\left({}^{t}d\right){}^{t}\psi_{0} + f\left(\bar{\alpha}\right)G_{V} \right]\mathbf{N}^{dT}\mathbf{N}^{d} + G_{V} l_{c}^{2}\mathbf{B}^{dT}\mathbf{B}^{d} \right\} dV \,, \tag{78}$$

and the vectors of the external forces, internal forces, and damage energy are [47,48,51]

$${}^{t+\Delta t}\mathbf{R} = \int_{V} \mathbf{N}^{uT}\, {}^{t+\Delta t}\mathbf{b} dV + \int_{A} \mathbf{N}^{uT}\, {}^{t+\Delta t}\mathbf{h} dA, \tag{79}$$

$${}^{t}\mathbf{F}^{u} = \int_{V} \theta\left({}^{t}d\right)\mathbf{B}^{uT}\, {}^{t}\boldsymbol{\sigma}_{0} dV \,, \tag{80}$$

$${}^{t}\mathbf{F}^{d} = \int_{V} \left\{ \mathbf{N}^{dT}\theta'\left({}^{t}d\right){}^{t}\psi_{0} + f\left(\bar{\alpha}\right)G_{V}\left[\mathbf{N}^{dT}\, {}^{t}d + \mathbf{B}^{dT} l_{c}^{2} \nabla\, {}^{t}d \right] \right\} dV \,. \tag{81}$$

Applying the Newton–Raphson iterative procedure (Eq. (3)) to solve the coupled system of nonlinear equations (Eq. (74)) yields [47,48,51]

$$\begin{bmatrix} {}^{t+\Delta t}\mathbf{K}^{uu(i-1)} & {}^{t+\Delta t}\mathbf{K}^{ud(i-1)} \\ {}^{t+\Delta t}\mathbf{K}^{du(i-1)} & {}^{t+\Delta t}\mathbf{K}^{dd(i-1)} \end{bmatrix} \begin{Bmatrix} \Delta\mathbf{U}^{(i)} \\ \Delta\mathbf{d}^{(i)} \end{Bmatrix} = \begin{Bmatrix} {}^{t+\Delta t}\mathbf{R} - {}^{t+\Delta t}\mathbf{F}^{u(i-1)} \\ -{}^{t+\Delta t}\mathbf{F}^{d(i-1)} \end{Bmatrix}, \tag{82}$$

Where the subscript *i* indicates the number of iterations. After each iteration, the total displacement and damage are calculated as [47,48,51]

$${}^{t+\Delta t}\mathbf{U}^{(i)} = {}^{t+\Delta t}\mathbf{U}^{(i-1)} + \Delta\mathbf{U}^{(i)}, \tag{83}$$

$${}^{t+\Delta t}\mathbf{d}^{(i)} = {}^{t+\Delta t}\mathbf{d}^{(i-1)} + \Delta\mathbf{d}^{(i)}. \tag{84}$$

For a staggered iterative solution scheme, the submatrices (Eqs. (76) and (77)) can be neglected, which provides a more stable solution for the coupled system, as presented in [47,48,51].

3 Experimental investigation

The same TiNi SMA material is investigated experimentally under full-loop and subloop loading conditions. For the experimental investigation [13], a rectilinear wire made of Ti–55.4-wt% Ni SMA, 0.75 mm in diameter, was used (Furukawa Electric Co). The wire is prepared through shape memory processing at 673 K for 60 min, followed by cooling in an electric furnace. The determined reverse transformation finish temperature T_{Af} was approximately 323K [13]. A tensile testing machine was used for the investigation, and an extensometer with a gauge length of 20 mm was used to measure the displacement. Full-loop loading and unloading were applied under a constant strain rate $d\varepsilon/dt = 1\%/\min$, as shown in Figure 3a.

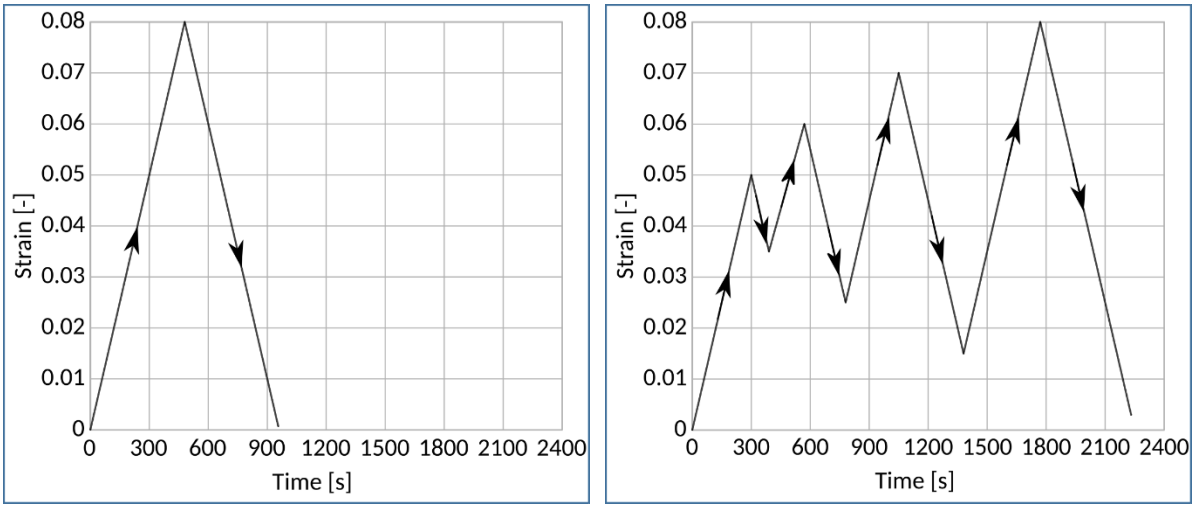

a) *b)*

Figure 3 Loading conditions for a) full-loop and b) subloop cases

The recorded stress–strain response is shown in Figure 4a. As shown in Figure 4a, stress plateaus appear in the loading and unloading processes. The stress plateau in the loading process is due to martensitic transformation, whereas those in the unloading process are due to reverse transformation from the martensite phase to the austenite phase. This is a typical stress–strain diagram of TiNi SMAs. Subloop loading conditions are applied at the same constant strain rate in further experimental investigations. During the loading process, before the completion of the martensitic transformation, the specimen is unloaded. Similarly, before the end of the reverse transformation, the specimen is reloaded again, as shown in Figure 3b. The stress–strain response is depicted in Figure 4b. The figure also shows the complex stress–strain diagram. Typical TiNi SMAs exhibit this type of response under subloop loading conditions. In particular, the stress plateau increases and decreases in a complex manner during the reloading process. This phenomenon occurs because the boundary between the martensite and austenite phases moves within the material during the loading and unloading processes. This complex behavior manifests because of the decreasing deformation resistance each time the boundary passes through the material [13]. In other words, this phenomenon occurs because of the accumulation of damage during cyclic loading.

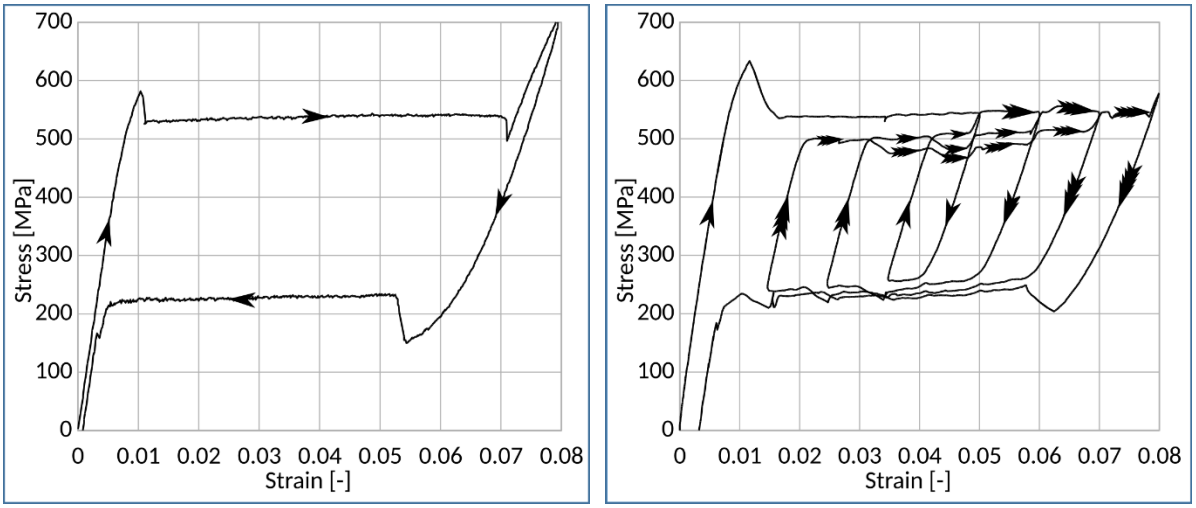

Figure 4 Stress–strain response for experimental investigation of TiNi SMA specimens a) full-loop loading; b) subloop loading [13]

4 Numerical verification

For numerical verification, we decided to demonstrate the TiNi SMA constitutive model, i.e., the PFDM implementation response at the unit cube example, which can be considered a wire segment. The unit dimensions are chosen to exclude the scale and FEM mesh sensitivity of the structure as respective variables and to demonstrate the functionality of the proposed solution. The material parameters are calibrated by manually fitting the stress–strain curves obtained by simulations and experimental investigation. For the experimental research, the same TiNi SMA material is used, but the stress–strain responses have slight differences in material parameters.

4.1 Different options for simulation of TiNi SMA behavior

The implementation of the theory in the FEM software is tested to show which option offers the best results. The observed simulation options are as follows:

1) the pure TiNi SMA constitutive model, without the PFDM, as described in subsection 2.1;

2) the TiNi SMA constitutive model with the PFDM presented in subsection 2.2 but without the fatigue function described using Eqs. (31)–(36);

3) all cases, i.e., the TiNi SMA constitutive model with the PFDM and fatigue function.

The simulations are performed using the same material parameters listed in Table 1 and Table 2. As shown in Figure 5, for both full-loop and subloop loading cases, the pure modified SMA constitutive model without the PFDM and fatigue function cannot satisfactorily capture the experimental response. The stress–strain hysteresis is constant and does not change during the loading–unloading cycles. For the case with the PFDM, the stress–strain response is the same for the full-loop loading case; however, a difference can be noticed in the case of subloop loading when the fatigue function is used. According to the behavior shown in Figure 5b, the fourth cycle stress plateau decreases because of the fatigue in the material described by Eqs. (35) and (36).

According to the damage–strain dependence depicted in Figure 6a, the fatigue function does not affect the accumulation of damage for the full-loop loading case. Conversely, in the subloop loading case (Figure 6b), in the fourth cycle, the damage increases during elastic reloading because the threshold value defined by Eq. (36) is achieved. Using the proposed PFDM–damage function implementation,

we can control the increase in damage in various regimes, allowing for good qualitative and quantitative simulation results in a real-world scenario.

The martensitic volume fraction value must be accurately computed because the amount of inelastic transformation strain is strongly related to the computed value according to Eq. (2). Figure 7 illustrates the martensitic volume fraction with respect to strain for all three simulation options. For both full-loop and subloop loading cases, we have the same diagrams for the PFDM implementation with and without the fatigue function. However, in the case of the pure TiNi SMA model, there is a slight difference: there are no residual strains after unloading because we established the relationship between the damage value and martensitic volume fraction.

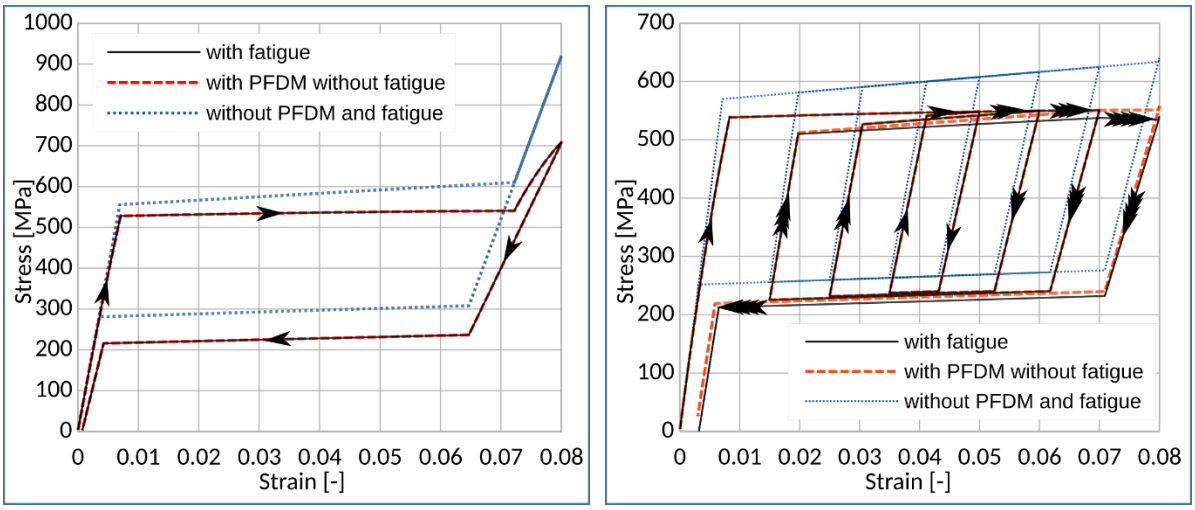

Figure 5 Stress–strain response for different options of PFDM and fatigue function implementation: a) full-loop loading; b) subloop loading

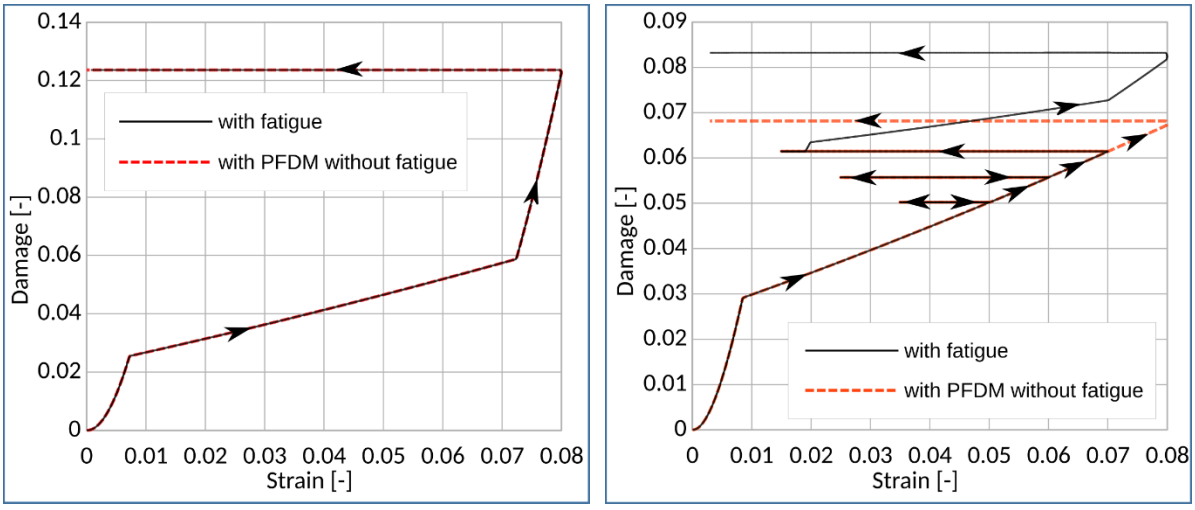

Figure 6 Damage–strain diagram for different options of PFDM and fatigue function implementation: a) full-loop loading; b) subloop loading

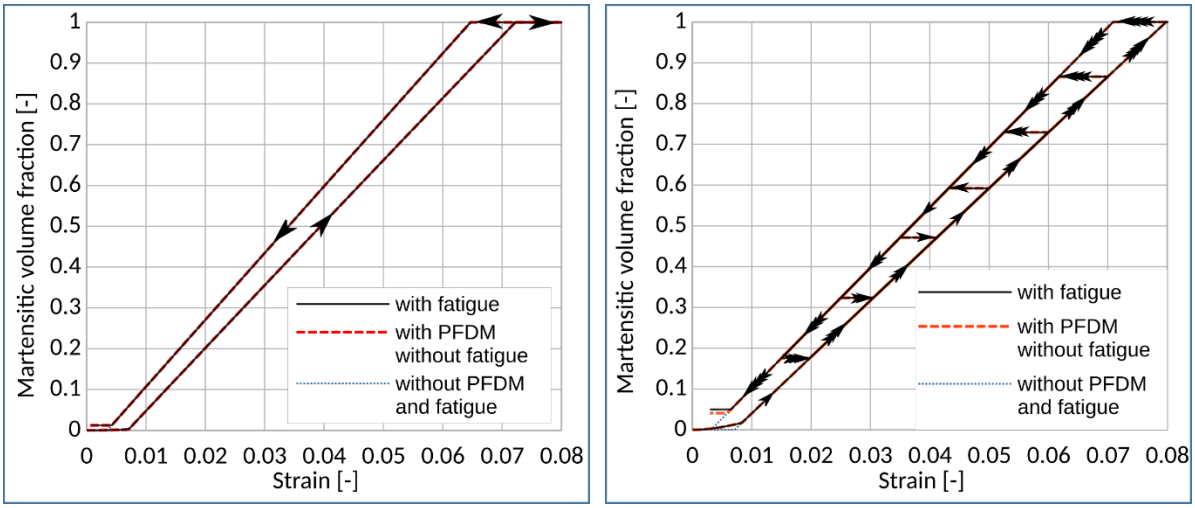

Figure 7 Martensitic volume fraction–strain diagram for different options of PFDM and fatigue function implementation: a) full-loop loading; b) subloop loading

4.2 Full-loop loading case verification

The unit cube is loaded by the prescribed displacement on one side, while the other is constrained in the loading direction (z-axis). The material parameters of TiNi SMA are calibrated to the experimental results and are listed in Table 1. Isothermal loading conditions are assumed at a constant temperature of $353K$, which is the same as that under experimental conditions. Loading–unloading is solved in 3200 equal time steps in a strain-controlled manner using the loading–unloading function. The stress–strain response is shown in Figure 8.

Table 1 Material parameters for one-element examples, full-loop loading [40]

E_A	E_M	α_A	α_M
80 GPa	40 GPa	$22.0 \cdot 10^{-6} K^{-1}$	$22.0 \cdot 10^{-6} K^{-1}$
T_{Ms}	T_{Mf}	T_{As}	T_{Af}
257 K	247 K	320 K	323 K
$H_{\max}$	ν	$\rho \Delta s_A$	$\rho \Delta s_M$
0.057	0.33	$-0.55 MPa\, K^{-1}$	$-0.35 MPa\, K^{-1}$
l_c	G_V	tol	T_{ref}
0.1 mm	150 MPa	1.e-7	353 K

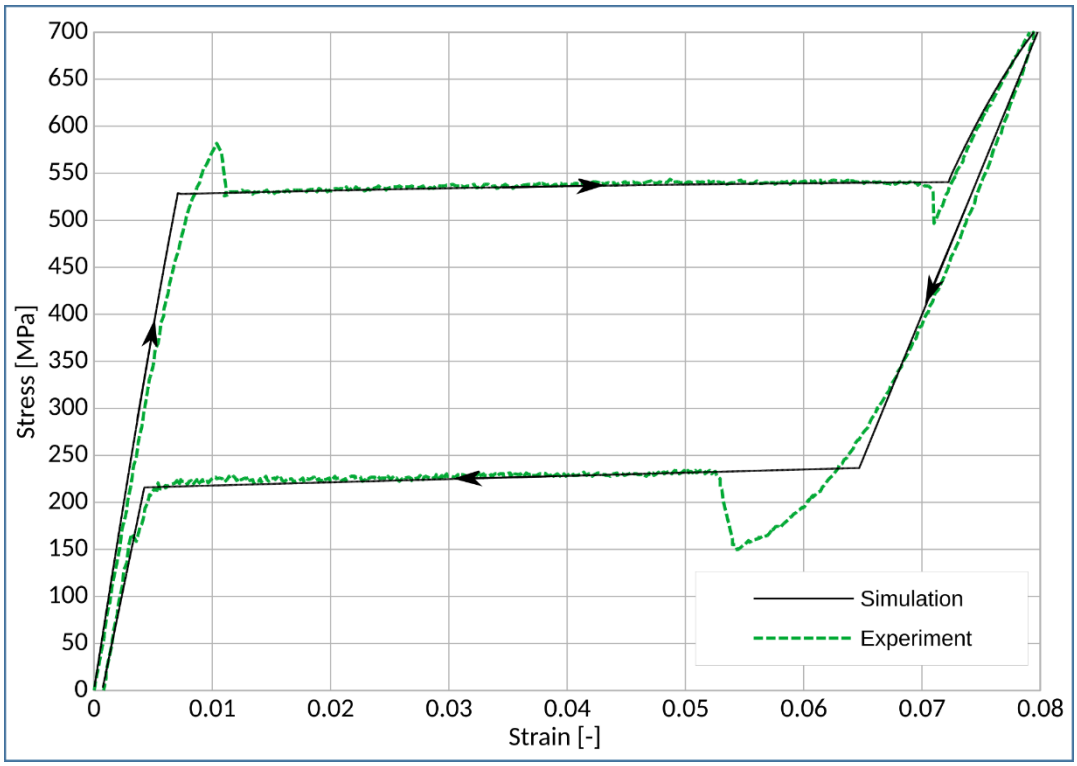

Figure 8 Comparison of experimental and simulation stress–strain response for full-loop loading case

4.3 Subloop loading case verification

The subloop loading is performed in four cycles according to the loading function shown in Figure 3b. Isothermal loading conditions are assumed at a constant temperature of $353K$ for the same reasons as those in the previous case. The example is solved in 7440 equal loading steps. The stress–strain response is shown in Figure 9.

Table 2 Material parameters for one-element examples, subloop loading [40]

E_A	E_M	α_A	α_M
80 GPa	40 GPa	$22.0 \cdot 10^{-6} K^{-1}$	$22.0 \cdot 10^{-6} K^{-1}$
T_{Ms}	T_{Mf}	T_{As}	T_{Af}
243 K	230 K	320 K	323 K
$H_{\max}$	ν	$\rho \Delta s_A$	$\rho \Delta s_M$
0.064	0.33	$-0.55 MPa\, K^{-1}$	$-0.35 MPa\, K^{-1}$
l_c	G_V	tol	T_{ref}
0.1 mm	140 MPa	1.e-7	353 K

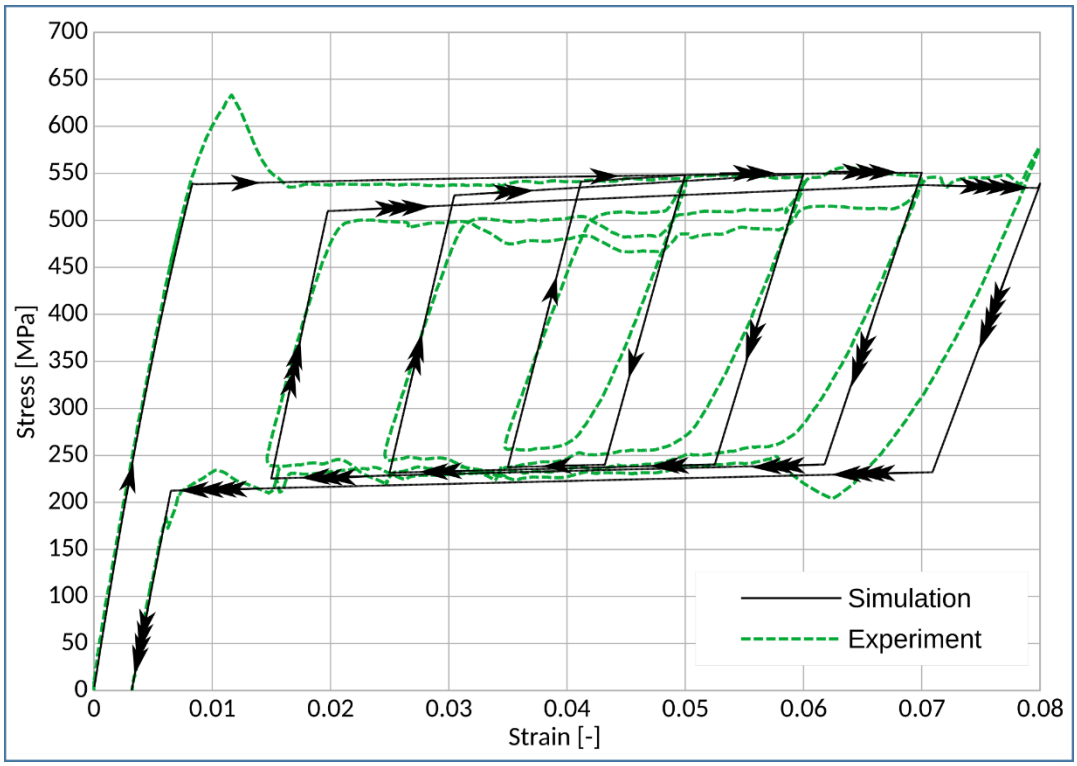

Figure 9 Comparison of experimental and simulation stress–strain response for subloop loading case

5 Simulation of NiTi SMA wire segment

After the calibration of the material parameters listed in Table 2, the wire segment is modeled according to the loading and boundary conditions during the experimental investigation described in Section 3. The segment of the TiNi SMA rectilinear wire is modeled in the 20-mm gauge length of the extensometer. One-eighth of the wire segment is modeled because of the symmetry.

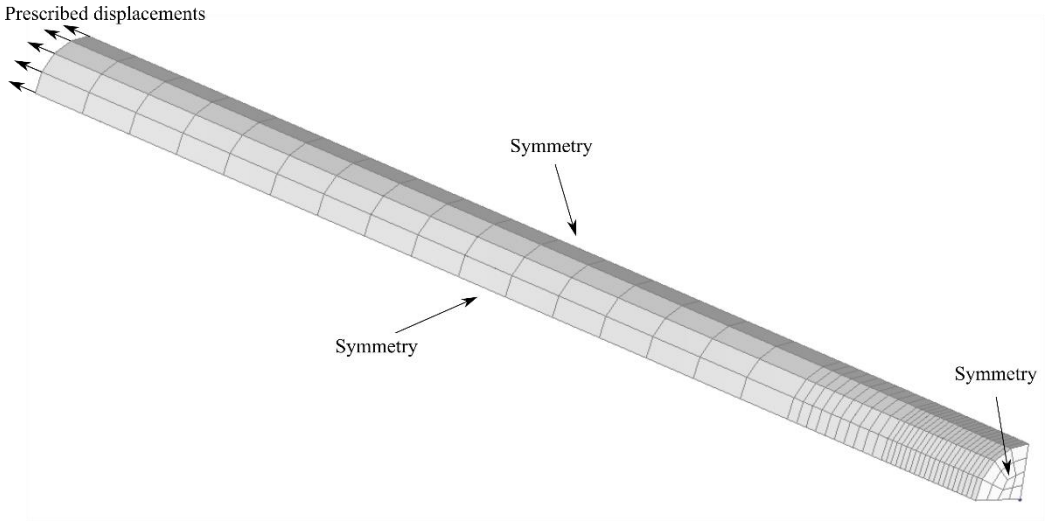

Figure 10 Finite element mesh of TiNi SMA wire segment with boundary and loading conditions

A finite element mesh is prepared to show the localization of the martensitic volume fraction and damage in the middle zone (Figure 10). The cross-section of the middle is reduced by 1%. In this zone, the finite element mesh discretization is finer, whereas it is coarser at the ends of the wire. The loading conditions are controlled using the prescribed displacements shown in Figure 3b. The force–displacement diagram is transformed into stress–strain by the following relations:

$$\sigma = \frac{F}{A_0}; \quad \varepsilon = \frac{\Delta l}{l_0}, \tag{85}$$

where F represents the total constrained force at the prescribed displacement nodes, A_0 denotes the nominal cross-sectional area of the wire, Δl denotes the elongation of the wire, and l_0 denotes the nominal length of the wire. The results are presented in Figure 11. The diagram is similar to the simulation results of the one-element example; however, some differences can be observed because of the localization of both the damage and martensitic volume fraction in the middle of the wire segment. After the initial linear elastic loading, a sudden decrease in stress can be observed because of the localization of the martensitic volume fraction in the middle of the specimen and its unequal propagation along the wire. However, after the initial instability, the stress–strain diagram becomes smooth and follows the results obtained from one-element simulations.

By analyzing the development of damage and martensitic volume fraction, the most interesting results at the end of the loading–unloading cycles are shown in Figure 12 and Figure 13. The points of interest are marked in Figure 11, where (a) and (b) denote the end of loading and unloading in the first cycle, (c) and (d) denote that in the second cycle, (e) and (f) denote that in the third cycle, and (g) and (h) denote that in the fourth cycle, respectively.

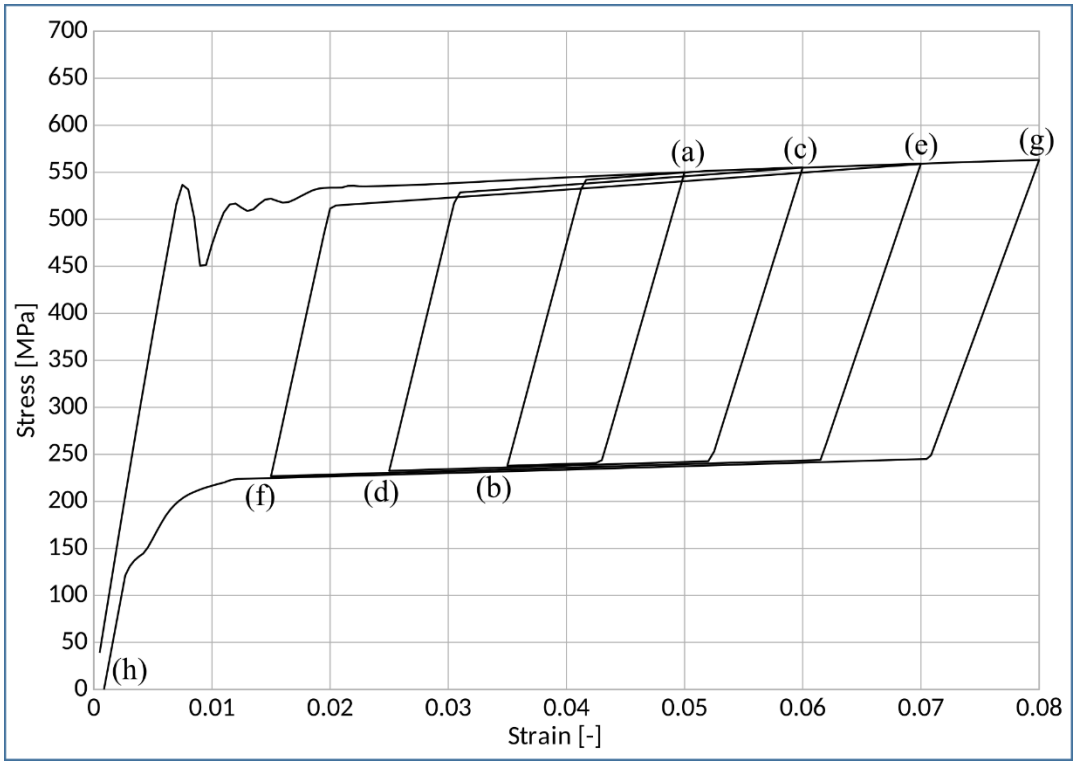

Figure 11 Stress–strain diagram for TiNi SMA wire segment loaded by prescribed displacements

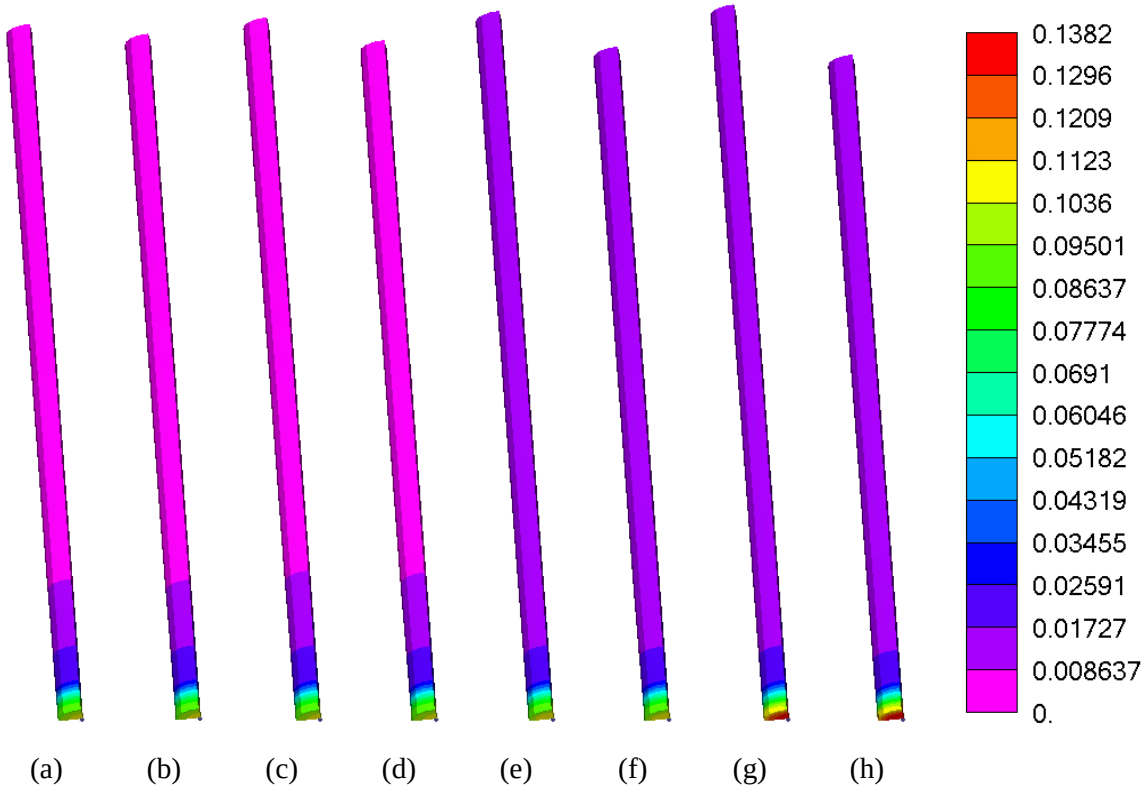

Figure 12 Damage to TiNi SMA wire segment at the end of loading–unloading cycles

In Figure 12, the damage field is given at points (a)–(h) denoted in Figure 11. Damage occurs in the middle of the specimen and increases after each cycle up to the maximal value localized at the middle of the wire segment.

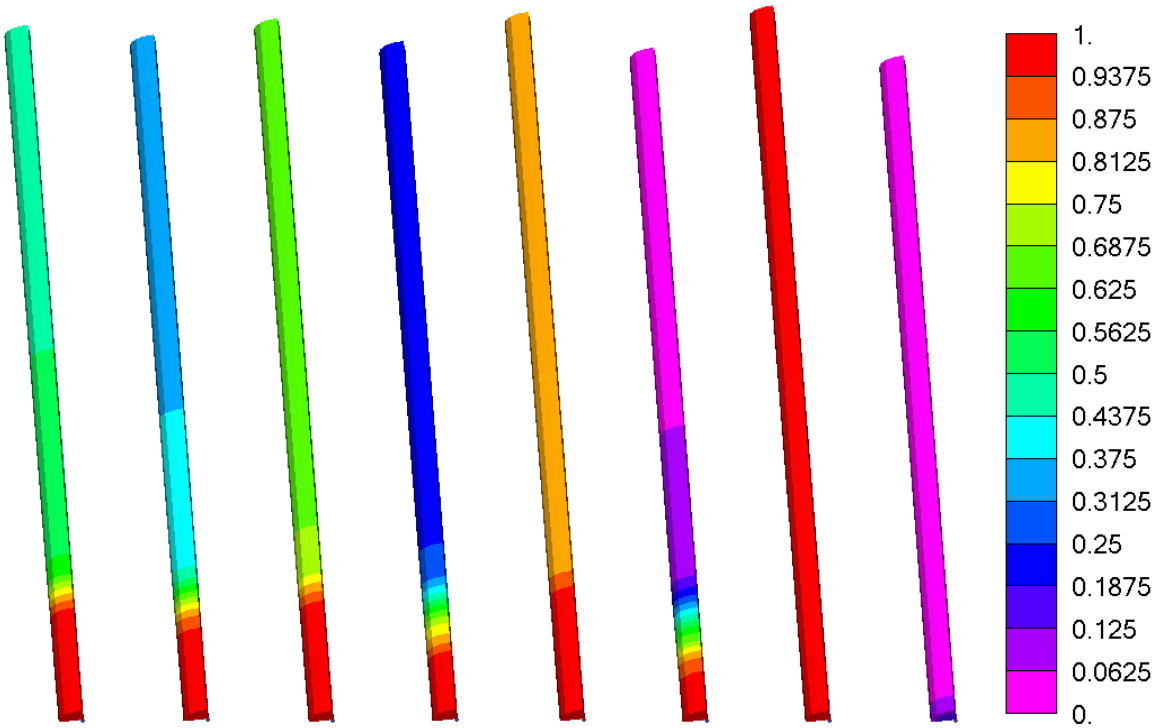

Figure 13 Martensitic volume fraction of TiNi SMA wire segment at the end of loading–unloading cycles

In Figure 13, the martensitic volume fraction field is shown at points (a)–(h) denoted in Figure 11. The development of martensite in the wire can be observed during loading, whereas unloading is followed by reverse transformation. As evident from the result, martensite phase initiates at the highest stressed locations during the loading process, and propagates along the specimen axis. During the unloading process, reverse transformation progresses backward from the last location where martensitic transformation occurred. This phenomenon aligns with a well-known behavior in TiNi SMA [57 - 60].

6 Discussion and conclusions

The investigation of TiNi SMAs is a source of exciting phenomena that should be described, and simulation techniques should be considered. In this study, the authors decided to extend the research toward subloop loading conditions, which are essential for many applications of TiNi SMA devices. Previously obtained experimental results have been reviewed, and new observations are presented.

According to the experimental results with respect to the obtained simulation results, under full-loop loading–unloading conditions, the maximal transformation strain is lower than that under subloop loading conditions because the elastic loading after martensitic transformation increases stress up to 700 MPa, whereas, in the case of subloop loading, the maximal stress after martensitic transformation is 570 MPa.

In addition to the maximal transformation strain, the martensitic start and finish temperatures are higher for full-loop loading than for subloop loading because the hardening of the material is strongly related to the maximal transformation strain.

The accumulated (residual) transformation strain after unloading is higher for subloop loading than for full-loop loading. The accumulation of the martensitic transformation strain is noticed in loading branches, where the elastic strain energy increases; thus, the subloop loading has repeated loading–unloading cycles, which results in a higher accumulation of transformation strain.

The relationship between the computed damage of the material and the accumulated martensitic transformation strain is of interest. This study demonstrates a different relationship between the full-loading and subloop loading cases. In the subloop loading case, 60% of the damage value is considered the accumulated martensitic transformation strain value. In contrast, in the case of full-loop loading, because of the strong increase in damage in the elastic branch after martensitic transformation, only 10% of the damage value is the accumulated martensitic transformation strain. These results are a topic of interest for further research and will be investigated in the future.

In the experimental investigation, the peaks can be observed at the beginning and end of the forward and reverse transformations. This behavior can be explained by the instability of the transformation process, accompanied by the appearance of Lüders bands. The proposed model cannot capture these peaks; however, these possibilities will be investigated in the future.

The authors proposed the PFDM as a cutting-edge numerical technique for the modified TiNi SMA constitutive model with the application of the fatigue function to simulate the change in stress–strain hysteresis during subloop loading and its influence on the accumulation of martensitic transformation strain. A relationship between damage and residual strain is proposed, and excellent qualitative and quantitative results are obtained.

7 Acknowledgment

This work is the result of a research visit of Vladimir Dunić to AIT, Japan, in the framework of the SAKURA science program. This research was supported by the Science Fund of the Republic of Serbia, #GRANT No 7475, Prediction of damage evolution in engineering structures - PROMINENT and by the University of Kragujevac project for young scientists Developing the procedure for damage simulation in metallic structures due to cyclic loading - DEEDS. The authors are grateful to Professor Hisaaki Tobushi for useful discussions and Professor Elzbieta Pieczyska for networking support.

8 Literature

[1] Qidwai MA, and Lagoudas DC. Numerical implementation of a shape memory alloy thermomechanical constitutive model using return mapping algorithms. *Int J Numer Meth Eng* 2000; 47: 1123-1168.

[2] Hartl DJ, and Lagoudas DC. Aerospace applications of shape memory alloys. *Proc Inst Mech Eng G* 2007; 221: 535-552.

[3] Song G, Ma N, and Li H-N. Applications of shape memory alloys in civil structures. *Eng Struct* 2006; 28: 1266-1274.

[4] Jani JM, Leary M, and Subic A. Shape memory alloys in automotive applications. *Appl Mech Mater* 2014; 663: 248-253.

[5] Dunić V. Shape memory alloys in automotive industry – overview, application, modeling. In: 8th International Congress Motor Vehicles & Motors, 2020 - Ecology - vehicle and road safety - Efficiency, Kragujevac, Serbia, October 8-9, 2020, pp 165-168.

[6] Das S, Sajeer MM, and Chakraborty A. Vibration control of horizontal axis offshore wind turbine blade using SMA stiffener. *Smart Mater Struct* 2019; 28: 095025.

[7] Savi MA, and Paiva A. Describing internal subloops due to incomplete phase transformations in shape memory alloys. *Arch Appl Mech* 2005; 74: 637-647.

[8] Tanaka K, Nishimura F, Hayashi T, et al. Phenomenological analysis on subloops and cyclic behavior in shape memory alloys under mechanical and/or thermal loads. *Mech Mater* 1995; 19: 281-292.

[9] Müller I, and Xu H. On the pseudo-elastic hysteresis. *Acta Metall Mater* 1991; 39: 263-271.

[10] Ortín J. Partial hysteresis cycles in shape-memory alloys: Experiments and modelling. *J Phys IV France* 1991; 1: C4-65.

[11] Boyd JG, and Lagoudas DC. A thermodynamical constitutive model for shape memory materials. part I. The monolithic shape memory alloy. *Int J Plast* 1996; 12: 805-842.

[12] Tanaka K, and Nagaki S. A thermomechanical description of materials with internal variables in the process of phase transitions. *Ing Arch* 1982; 51: 287-299.

[13] Tobushi H, Ikawa T, and Matsui R. Pseudoviscoelastic behavior of TiNi shape memory alloy in subloop. *T MRS Jap* 2003; 28: 611-614.

[14] Savi MA, Paiva A, Baeta-Neves AP, et al. Phenomenological modeling and numerical simulation of shape memory alloys: A thermo-plastic-phase transformation coupled model. *J Intell Mater Syst Struct* 2002; 13: 261-273.

[15] Baêta-Neves AP, Savi MA, and Pacheco PMCL. On the Fremond's constitutive model for shape memory alloys. *Mech Res Commun* 2004; 31: 677-688.

[16] Paiva A, Savi MA, Braga AMB, et al. A constitutive model for shape memory alloys considering tensile-compressive asymmetry and plasticity. *Int J Solids Struct* 2005; 42: 3439-3457.

[17] Phillips FR, Wheeler RW, Geltmacher AB, et al. Evolution of internal damage during actuation fatigue in shape memory alloys. *Int J Fatigue* 2019; 124: 315-327.

[18] Scalet G, Karakalas A, Xu L, et al.. Finite strain constitutive modelling of shape memory alloys considering partial phase transformation with transformation-induced plasticity. *Shape Mem Superelasticity* 2021; 7: 206-221.

[19] Karakalas AA, Machairas TT, and Saravanos DA. Effect of shape memory alloys partial transformation on the response of morphing structures encompassing shape memory alloy wire actuators. *J Intell Mater Syst Struct* 2019; 30: 1682-1698.

[20] Ortın J, and Delaey L. Hysteresis in shape-memory alloys. *Int J Non Linear Mech* 2002; 37: 1275-1281.

[21] Ren W, Li H, and Song G. Phenomenological modeling of the cyclic behavior of superelastic shape memory alloys. *Smart Mater Struct* 2007; 16: 1083-1089.

[22] Wang J *Constitutive Modeling of the Thermomechanical and Cyclic Behavior of Shape Memory Alloys in Finite Deformations*, PhD thesis, ENSTA-ParisTech/Universite PARIS-SACLAY, 2017.

[23] Wang B, Kang G, Kan Q, et al. Atomistic study on the super-elasticity of nanocrystalline NiTi shape memory alloy subjected to a cyclic deformation. *Comput Mater Sci* 2018; 152: 85-92.

[24] Xiao Y, Zhou M, Zeng P, et al. Phenomenological modeling on cyclic deformation of superelastic NiTi shape memory alloy. *Mater Res Express* 2019; 6: 075703.

[25] Xiao Y, Zeng P, and Lei L. A microstructure-based constitutive model accounting for rate dependence of superelastic NiTi alloy under cyclic deformation. *J Intell Mater Syst Struct* 2020; 31: 17-39.

[26] Xiao Y, and Jiang D. Constitutive modelling of transformation pattern in superelastic NiTi shape memory alloy under cyclic loading. *Int J Mech Sci* 2020; 182: 105743.

[27] Xie X, Kang G, Kan Q, et al. Phase field modeling for cyclic phase transition of NiTi shape memory alloy single crystal with super-elasticity. *Comput Mater Sci* 2018; 143: 212-224.

[28] Xie X, Kang G, Kan Q, et al. Phase-field theory based finite element simulation on thermo-mechanical cyclic deformation of polycrystalline super-elastic NiTi shape memory alloy. *Comput Mater Sci* 2020; 184: 109899.

[29] Choi H, Lim HJ, and Yun GJ. An integrated unified elasto-viscoplastic fatigue and creep damage model with characterization method for structural analysis of nickel-based high-temperature structure. *Int J Damage Mech* 2023; 32: 73-102.

[30] Kan Q, Qiu B, Zhang X, et al. Thermo-mechanically coupled functional fatigue of NiTi shape memory alloys under multiaxial cyclic loadings. *Int J Fatigue* 2023; 172: 107657.

[31] Kan Q, Zhang Y, Xu Y, et al. Tension-compression asymmetric functional degeneration of super-elastic NiTi shape memory alloy: Experimental observation and multiscale constitutive model. *Int J Solids Struct* 2023; 280: 112384.

[32] Kan Q, Zhang Y, Shi W, et al. Functional fatigue of superelasticity and elastocaloric effect for NiTi springs. *Int J Mech Sci* 2024; 265: 108889.

[33] Simoes M, and Pañeda EM. Phase field modelling of fracture and fatigue in shape memory alloys. *Comput Methods Appl* 2021; 373: 113504.

[34] Simoes M, Braithwaite C, Makaya A et al. Modelling fatigue crack growth in shape memory alloys. *Fatigue Fract Eng Mat Struct* 2022; 45: 1243-1257.

[35] Carrara P, Ambati M, Alessi R, and Lorenzis LD. A framework to model the fatigue behavior of brittle materials based on a variational phase-field approach. *Comput Methods Appl* 2020; 361: 112731.

[36] Dunić V *Development and Implementation of Thermo-Mechanical Constitutive Model for Numerical Analysis of Shape Memory Alloys*. PhD thesis, Faculty of Engineering, University of Kragujevac, Serbia, May 2015.

[37] Dunić V, and Slavković R. Implicit stress integration procedure for large strains of the reformulated shape memory alloys material model. *Continuum Mech Thermodyn* 2020; 32: 1287-1309.

[38] Lagoudas D *Shape Memory Alloys: Modeling and Engineering Applications*, Springer, 2010.

[39] Holzapfel GA *Nonlinear Solid Mechanics: A Continuum Approach for Engineering*, Chichester: John Wiley & Sons, 2000.

[40] Lagoudas D, Bo Z, Qidwai M, et al. *SMA–UM: User Material Subroutine for Thermomechanical Constitutive Model of Shape Memory Alloys*. Technical Report, Texas A&M University, College Station, TX, 2003.

[41] Kojić M, and Bathe KJ. Inelastic analysis of solids and structures. *Comp Fluid Solid Mech*, Berlin: Springer-Verlag Berlin and Heidelberg GmbH KG 2005.

[42] Kojić M, Vlastelica I, and Živković M. Implicit stress integration procedure for small and large strains of the Gurson material model. *Int J Numer Meth Eng* 2002; 53: 2701-2720.

[43] Miehe C, Hofacker M, and Welschinger F. A phase field model for rate-independent crack propagation: Robust algorithmic implementation based on operator splits. *Comput Methods Appl* 2010; 199: 2765-2778.

[44] Miehe C, Welschinger F, and Hofacker M. Thermodynamically consistent phase-field models of fracture: Variational principles and multi-field FE implementations. *Int J Numer Meth Eng* 2010; 83: 1273-1311.

[45] Molnár G, and Gravouil A. 2D and 3D Abaqus implementation of a robust staggered phase-field solution for modeling brittle fracture. *Finite Elem Anal Des* 2017; 130: 27-38.

[46] Pañeda EM, Golahmar A, and Niordson CF. A phase field formulation for hydrogen assisted cracking. *Comput Methods Appl* 2018; 342: 742-761.

[47] Živković J, Dunić V, Milovanović V, et al.. A modified phase-field damage model for metal plasticity at finite strains: Numerical development and experimental validation. *Metals* 2021; 11: 47.

[48] Živković J. *Improvement, Implementation and Experimental Verification of Phase-Field Modeling of Damage and Fracture in metals*. PhD thesis, University of Kragujevac, 2022.

[49] Molnár G, and Gravouil A. 2D and 3D Abaqus implementation of a robust staggered phase-field solution for modeling brittle fracture. *Finite Elem Anal Des* 2017; 130: 27-38.

[50] Pañeda EM, Golahmar A, and Niordson CF. A phase field formulation for hydrogen assisted cracking. *Comput Methods Appl*; M2018: 742-761.

[51] Dunić V, Živković J, Milovanović V, et al. Two-intervals hardening function in a phase-field damage model for the simulation of aluminum alloy ductile behavior. *Metals* 2021; 11: 1685.

[52] Dunić V, Busarac N, Slavković V, et al. A thermo-mechanically coupled finite strain model considering inelastic heat generation. *Continuum Mech Thermodyn* 2016; 28: 993-1007.

[53] Dunić V, Pieczyska EA, Tobushi H, et al. Experimental and numerical thermo-mechanical analysis of shape memory alloy subjected to tension with various stress and strain rates. *Smart Mater Struct* 2014; 23: 055026.

[54] Pieczyska EA, Staszczak M, Dunić V, et al. Development of stress-induced martensitic transformation in TiNi shape memory alloy. *J Mater Eng Perform* 2014; 23: 2505-2514.

[55] Kojić M, Slavković R, Živković M, et al. *PAK-S, Program for FE Structural Analysis*. *Faculty of Mechanical Engineering*. University of Kragujevac, Kragujevac, 1999.

[56] Bathe KJ. *Finite Element Procedures*. Cambridge, MA: K.-J. Bathe, 2014.

[57] Tanaka K. A thermomechanical sketch of shape memory effect: One-dimensional tensile behavior, *Res Mech* 1986; 18: 251–263.

[58] Tanaka K, Kobayashi S, Sato Y. Thermomechanics of transformation pseudoelasticity and shape memory effect in alloys. *Int J Plasticity* 1986; 2: 59-72.

[59] Tobushi H, Matsui R, Takeda K, et al. *Mechanical properties of Shape Memory Materials*. Nova Science Publishers, 2013.

[60] Sun Q, Matsui R, Takeda K, et al. *Advances in shape memory materials*, Springer, 2017.